Pore conformations and gating mechanism of a Cys-loop receptor

Yoav Paas*†‡, Gilad Gibor†, Regis Grailhe§, Nathalie Savatier-Duclert*, Virginie Dufresne*, Morten Sunesen¶, Lia Prado de Carvalho*, Jean-Pierre Changeux*‡, and Bernard Attali†‡

*Récepteurs et Cognition, Unité de Recherche Associée 2182 Centre National de la Recherche Scientifique, Institut Pasteur, 25 Rue du Docteur Roux, 75724 Paris Cedex 15, France; †Department of Physiology and Pharmacology, Sackler Medical School, Tel Aviv University, Tel Aviv 69978, Israel; §Institut Pasteur Korea, Sungbuk-gu, 39-1 Hawolgok-dong, Seoul 136-791, Korea; and ¶Sophion Bioscience A/S, Baltorpvej 154, DK-2750 Ballerup, Denmark

Contributed by Jean-Pierre Changeux, September 7, 2005

Neurons regulate the propagation of chemoelectric signals throughout the nervous system by opening and closing ion channels, a process known as gating. Here, histidine-based metal-binding sites were engineered along the intrinsic pore of a chimeric Cys-loop receptor to probe state-dependent Zn^{2+}-channel interactions. Patterns of Zn^{2+} ion binding within the pore reveal that, in the closed state, the five pore-lining segments adopt an oblique orientation relative to the axis of ion conduction and constrict into a physical gate at their intracellular end. The interactions of Zn^{2+} with the open state indicate that the five pore-lining segments should rigidly tilt to enable the movement of their intracellular ends away from the axis of ion conduction, so as to open the constriction (i.e., the gate). Alignment of the functional results with the 3D structure of an acetylcholine receptor allowed us to generate structural models accounting for the closed and open pore conformations and for a gating mechanism of a Cys-loop receptor.

ion channel | membrane protein | structure | acetylcholine

The highly homologous Cys-loop receptors are pentameric integral-membrane receptors that convert binding of neurotransmitters such as acetylcholine (ACh), serotonin, glycine, and GABA into opening and closing of an intrinsic ionic channel (Fig. 6*A*, which is published as supporting information on the PNAS web site) (1–4). Based on 3D structures resolved by EM at 9- and 4-Å resolution, the five pore-lining helices (M2 segments; Fig. 6 *A–C*) of the ACh receptor (AChR) were said to kink at positions 9′ and 13′ toward the axis of ion conduction and to form a "hydrophobic girdle" that obstructs ionic flow at rest (5, 6). It was further proposed that, upon activation, symmetric rotations of the M2 segments around their longitudinal axis move the kinks sideways, thereby opening the hydrophobic girdle to enable ionic flow (5, 6). Asymmetric gating rotations were suggested in the case of a $GABA_A$ receptor (7). In contrast, substituting cysteines along the pore of the muscle AChR and determination of their accessibility to methanethiosulfonates showed that the activation gate is close to position −1′ (8), near the bottom of the pore (Fig. 6 *A–C*). Because similar patterns of accessibility to methanethiosulfonates were probed in the closed and open states, rotational movements of the pore-lining helices have been excluded (8, 9), but no alternative gating motions have been suggested thus far. Here, state-dependent interactions of Zn^{2+} with histidines (His) substituted along the pore of a chimeric Cys-loop receptor allowed us to localize the activation gate, to probe tilting gating motions, and to elaborate homology 3D models that account for the activity-dependent orientation of the pore-lining segments.

Materials and Methods

Mutagenesis. See *Supporting Materials and Methods* in *Supporting Text*, which is published as supporting information on the PNAS web site.

Electrophysiology in *Xenopus* Oocytes. Stage V and VI *Xenopus* oocytes were prepared as described in ref. 10. Expression of channel constructs was obtained by injecting 10 nl of cDNA vector directly into *Xenopus* oocyte nuclei (1 ng). Two-electrode voltage-clamp measurements were performed at 22–24°C 2–5 days after DNA microinjection, as described in ref. 10. Details regarding the perfusion conditions and data acquisition are provided in *Supporting Materials and Methods* in *Supporting Text*.

Selectivity Determinations in HEK-293 Cells and Model Building. See *Supporting Materials and Methods* in *Supporting Text*.

Results

Basic Properties of the Chimeras. The homopentameric α7–$5HT_{3A}$ chimeric receptor (11) was used here to generate nondesensitizing receptor mutants that carry low-affinity metal-binding sites exposed to the pore lumen. Preliminary considerations related to chimeric design, Zn^{2+}–protein interactions, and glycine (Gly) substitutions as controls are discussed in *Note 1* in *Supporting Text*. The chimeras were expressed in *Xenopus* oocytes that were subjected to fast and constant perfusion (*Materials and Methods*). Dose-dependent activation (e.g., Fig. 6*D Right*) allowed us to plot dose–response isotherms and to calculate apparent affinities (EC_{50} values) (Table 1). Compared with the α7–$5HT_{3A}$R basic chimera, all of the His-containing chimeras displayed slightly higher affinity for ACh and significantly higher cooperativity (n_H values in Table 1), indicating that ACh stabilizes the active state but not the so-called "pathological open-desensitized state" (see *Note 2* in *Supporting Text*). Except for two cases, the time course of activation of the various chimeras was similar to that of the α7–$5HT_{3A}$R basic chimera (Table 1). In contrast, L9′H and L9′G substitutions dramatically slowed activation (Table 1). Testing the ionic selectivity of three representative chimeras (H−5′, H−4′, and H−2′) revealed that they became largely permeable to Cl^- ions (*Note 3* in *Supporting Text*).

The Effect of External Zn^{2+} on Conduction Through the Open Pore. In postapplication protocols, where Zn^{2+} was externally applied after reaching steady-state activation by saturating concentrations of ACh, the currents declined to a steady-state inhibition to an extent and at a rate that depended on Zn^{2+} concentration (Fig. 1 *A* and *B*). Dose–response isotherms (e.g., Fig. 1*C*) provided the Zn^{2+} inhibition constants (K_i) (Table 1). Gly-containing controls showed a low background inhibition (Fig. 1 *D* and *E* and Table 1), indicating that the inhibition is specific to interactions of Zn^{2+} with the substituting histidines. In one case (chimera H−4′), Zn^{2+} potentiated the steady-state currents (Table 1).

Abbreviations: ACh, acetylcholine; AChR, ACh receptor; OB, open blocked.

‡To whom correspondence may be addressed. E-mail: yopaas@netvision.net.il, changeux@pasteur.fr, or battali@post.tau.ac.il.

Table 1. Basic properties of histidine-containing chimeras and their glycine-containing controls

M1 ← -5′ -2′ 2′ 6′ 9′ 13′ 16′ → M2	ACh EC_{50}, μM*	n_H	$\tau_{activation}$, ms†	Zinc K_i, μM, or [percent inhibition]‡
GluClβR: FWI..DLHSTAGRVALGVTTLLTMTTMQSAINA				
α7-5HT$_{3A}$R: FCLPPD..SG.ERVSFKITLLLGYSVFLIIVSD	68 ± 24 (7)	1.4 ± 0.2	101 ± 22 (7)	ND§
H-5′: ------LHSTAG----------T-------	10 ± 2.8 (6)	2.2 ± 0.3	66 ± 15 (15)	30 ± 4.8 (8)
G-5′: ------LGSTAG----------T-------	16 ± 2.0 (7)	3.2 ± 0.2	67 ± 17 (11)	[27 ± 2.0]% (5)
H-4′: ------LSHTAG----------T-------	7 ± 0.8 (7)	2.3 ± 0.4	97 ± 17 (8)	Potentiation¶
G-4′: ------LSGTAG----------T-------	ND	ND	80 ± 31 (6)	[42 ± 2.0]% (4)
H-3′: ------LSTHAG----------T-------	19 ± 4.7 (6)	1.6 ± 0.1	91 ± 18 (5)	480 ± 154 (5)‖
G-3′: ------LSTGAG----------T-------	ND	ND	75 ± 14 (4)	[28 ± 4.0]% (4)
H-2′: ------LSTAHG----------T-------	5 ± 0.5 (5)	2.4 ± 0.2	74 ± 28 (10)	80 ± 12 (6)
G-2′: ------LSTAGG----------T-------	15 ± 3.0 (7)	2.1 ± 0.1	68 ± 10 (9)	[19 ± 5.6]% (4)
H-1′: ------LSTAGH----------T-------	5 ± 0.3 (4)	2.9 ± 0.3	63 ± 22 (8)	54 ± 9.0 (5)
G-1′: ------LSTAGG----------T-------	15 ± 3.0 (7)	2.1 ± 0.1	68 ± 10 (9)	[19 ± 5.6]% (4)
H+2′: ------LSTAGG--H----------T-------	22 ± 1.0 (6)	1.8 ± 0.1	134 ± 22 (8)	47 ± 10 (5)
G+2′: ------LSTAGG--G----------T-------	ND	ND	136 ± 52 (6)	[16 ± 5.0]% (3)
H+6′: ------LSTAGG------H------T-------	NF**			
G+6′: ------LSTAGG------G------T-------	11 ± 2.6 (3)	2.3 ± 0.3	63 ± 11 (3)	[18 ± 3.0]% (3)
H+9′: ------LSTAGG---------H---T-------	17 ± 3.0 (5)	2.5 ± 0.3	561 ± 193 (10)†† 8527 ± 3872	30 ± 12 (6)
G+9′: ------LSTAGG---------G---T-------	ND	ND	365 ± 103 (6)‡‡ 2042 ± 599	[20 ± 5.0]% (3)
H+16′: ------LSTAGG-------------T--H----	5 ± 0.9 (5)	2.0 ± 0.3	97 ± 7 (5)	[28 ± 3.0]% (4)
G+16′: ------LSTAGG-------------T--G----	ND	ND	135 ± 10 (3)	[26 ± 1.0]% (3)

Dots within the sequence alignment correspond to gaps; hyphens reflect the same residue as appears in the aligned 5HT$_{3A}$R sequence (of α7-5HT$_{3A}$R).
*Apparent affinity as determined by the ACh concentration that gives half of the maximal current response. The number of tested oocytes is provided in parentheses and applies also for the number of Hill-coefficient (n_H) determinations.
†Time constant of activation of currents measured at −80 mV in ms (see *Supporting Materials and Methods* in *Supporting Text* for determination procedure).
‡Zinc inhibition constants (K_i) as derived from inhibition isotherms (e.g., Fig. 1*C*) plotted with steady-state inhibition data. The percentage of inhibition at 1 mM zinc, which is too low for curve fitting, is shown in brackets for chimeras displaying background inhibition.
§Not determined.
¶Maximally potentiated by 34 ± 10% at 50 μM. Compared to chimera G-4′, $P < 0.00001$.
**Not functional.
‖Significantly differs from the K_i value corresponding to chimera H-2′, $P < 0.015$.
††Significantly differs from the $\tau_{activation}$ of the α7–5HT$_{3A}$R, $P < 0.0005$.
‡‡Significantly differs from the $\tau_{activation}$ of the α7–5HT$_{3A}$R, $P < 0.015$.

Voltage Dependence of the Inhibition Exerted by External Zn^{2+}. The effect of membrane voltage on the inhibition by Zn^{2+} was examined on chimeras H−5′ and H−2′; it revealed that the rate and extent of current decline increase with membrane hyperpolarization (Fig. 7 *A* and *C*, which is published as supporting information on the PNAS web site). Current-voltage (*I–V*) relations (e.g., Fig. 7 *B* and *D*) allowed us to plot the Zn^{+2}-inhibition constant (K_i) as a function of membrane voltage (Fig. 7*I*). This analysis demonstrates a clear dependence of the apparent affinity for Zn^{2+} on membrane voltage. Under all voltages, only low background inhibition was displayed by the Gly-containing controls (Fig. 7 *E–H*).

At extremely negative membrane voltages (−140 mV and below), washing out ACh and Zn^{2+} resulted in robust inward currents, hereafter termed "off-response" currents (Fig. 2 *A–E*). The off-response currents became larger with hyperpolarization. The decay of the off-response currents was slow as long as very negative voltage was applied. Upon returning to −80 mV (e.g., Fig. 2*A*, arrow), the currents declined rapidly (Fig. 2 *A–E*). Fig. 2*F* shows that the ratio between the off-response amplitude and the current that was lost upon declining to a steady-state inhibition is linearly proportional to the membrane voltage. Note that none of the Gly-containing controls displayed off responses (Fig. 8, which is published as supporting information on the PNAS web site).

Effects Exerted by Zn^{2+} Applied Externally Before Channel Activation. Fig. 3*A* shows that coapplication of ACh and Zn^{2+} (black trace) to oocytes expressing chimera H−2′ results in a transient current that rapidly declines. The peak of this transient current reached ≈50% of the steady-state current elicited by ACh alone (gray trace), indicating that at least half of the channels opened and immediately became blocked. The amplitude of the off response accompanying this transient current was ≈20% of the steady-state currents elicited by ACh alone (Fig. 3*A Inset*, leftmost bar). In contrast, external applications of Zn^{2+} for 6, 2, and 0.5 s before the coapplication abolished the transient current completely (Fig. 3*A*, green, blue, and red traces, frontal to the black trace; Fig. 3*B*, all traces except the gray one). Yet, small, slowly progressing inward current was observed when adding ACh; it reached a steady-state inhibition and resulted in a small off response upon washout. These off responses were significantly smaller than the off-response amplitudes recorded in postapplication experiments (Fig. 3*A Inset*). Fig. 3*B* shows that application of Zn^{2+} before the coapplication leads to off responses that increase proportionally to the time of ACh addition until reaching saturation (*Inset*). When prolonged application of Zn^{2+} is immediately followed by washout (i.e., without adding ACh), no off responses could be seen (Fig. 3*C*), indicating that leak currents do not play a role (discussed below).

We then quantitatively monitored the kinetics of activation when Zn^{2+} was applied before the application of ACh alone (Fig. 4). Because the entire volume of the bath was replaced within 1.5–1.7 s (*Supporting Materials and Methods* in *Supporting Text*), Zn^{2+} first became equilibrated around the oocyte (6-s application) and then was washed out at the beginning of the ACh application phase, which lasted at least 12 s (Fig. 4). In the case of chimeras H−5′, H−2′, and H+2′, control activation (without

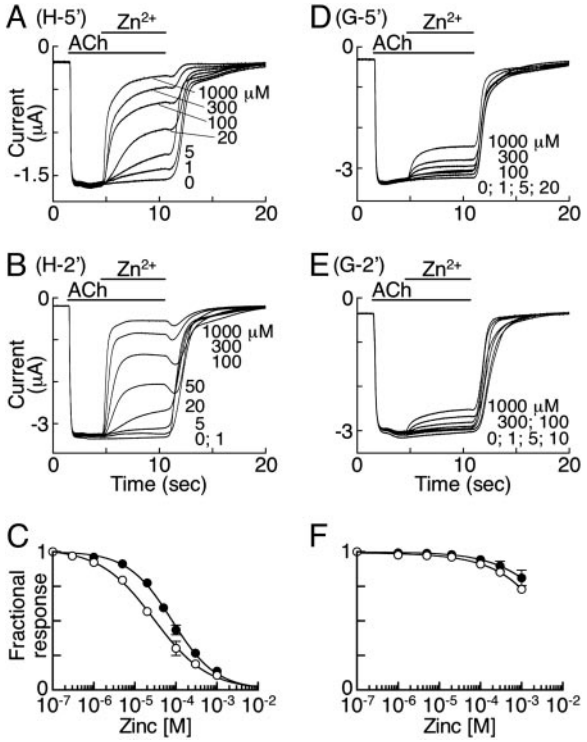

Fig. 1. Effects of Zn^{2+} applied externally after steady-state activation by ACh is achieved (Zn^{2+} postapplication). (*A*, *B*, *D*, and *E*) Representative current traces of chimeras containing histidines (*A* and *B*) or glycines (*D* and *E*) at the indicated positions. ACh, 300 μM (saturating concentration); Zn^{2+}, increasing μM concentrations as depicted. (*C*) Dose–response isotherms expressing fractional responses as a function of Zn^{2+} concentrations. Open circles, chimera H−5′; filled circles, chimera H−2′. (*F*) Inhibition isotherms corresponding to the control mutants. Open circles, G−5′; filled circles, G−2′. Data were fitted with a nonlinear regression to the Hill equation (*Supporting Materials and Methods* in *Supporting Text*). All recordings were performed at −80-mV holding potential.

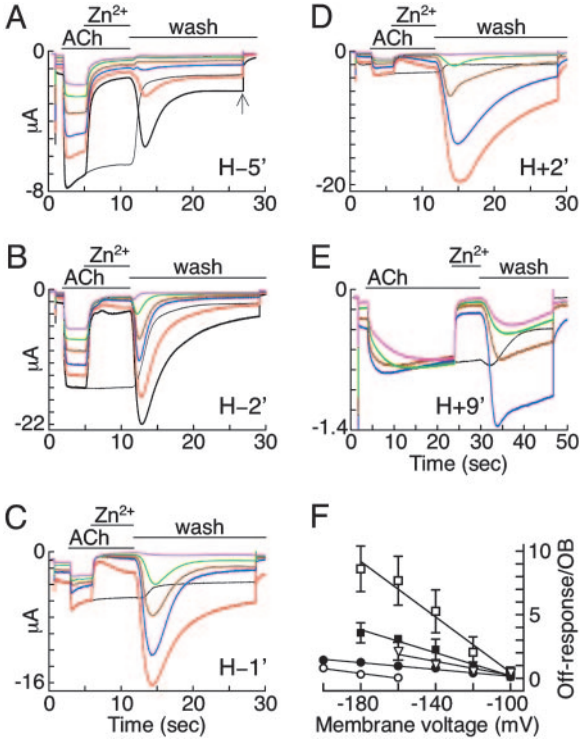

Fig. 2. Effect of membrane voltage on off-response currents. (*A–E*) Representative current traces recorded for the indicated chimeras. ACh, 300 μM; externally applied Zn^{2+}, 1 mM; wash, physiological solution (ND96). Color code for holding voltages in mV is as follows: magenta, −100; green, −120; brown, −140; blue, −160; red, −180; black, −200. The gray traces correspond to steady-state activation currents elicited by ACh at −200 (*A* and *B*), −180 (*C* and *D*), and −160 (*E*) mV. (*F*) Linear regression of the ratio of off-response peak currents over the OB population plotted as a function of membrane voltage. OB is calculated by subtracting the current observed at steady-state inhibition from the current of steady-state activation (i.e., the current lost due to the block). Error bars correspond to SD of at least five independent experiments.

preceding application of Zn^{2+}) was largely monophasic with fast kinetics (Fig. 4 *A–C*, gray traces; see also τ_1 values in Table 2, which is published as supporting information on the PNAS web site). In contrast, preceding application of Zn^{2+} was followed by biphasic activation responses to ACh, with fast and slow time courses (Fig. 4 *A–C*, black traces; see also $\tau_{1(zinc)}$ and $\tau_{2(zinc)}$ values in Table 2). The Gly-containing controls were not affected by preceding application of Zn^{2+} (Fig. 4 *E–G*), indicating that the different slow activation rates ($\tau_{2(zinc)}$) displayed by chimeras H−5′, H−2′, and H+2′ are specific to interactions of Zn^{2+} with the engineered histidines.

As to chimera H+9′, two slow kinetic components characterize its activation without or with preceding application of Zn^{2+} (Fig. 4*D*, gray and black traces, respectively). The time constants (Table 2) show that Zn^{2+} exerts little effect on the slow component (τ_1 vs. $\tau_{1(zinc)}$) and no effect on the slower component (τ_2 vs. $\tau_{2(zinc)}$). Hyperpolarization increased the activation rates of chimera H+9′ (Fig. 2*E*), without or with preceding application of Zn^{2+} to the same extent (data not shown). The slow activation of chimera G+9′ (Fig. 4*H*), which was observed with or without preceding application of Zn^{2+}, indicates that a mutation at position 9′ (in combination with V13′T) stabilizes the resting state.

Discussion

Zn^{2+} Blocks the Open State, Depending on the Location of the Substituting Histidines. The data presented in Figs. 1 and 7 indicate that externally applied Zn^{2+} moves in the pore solvent, where it becomes sensitive to changes in the electric field of the membrane, and occludes the open pore by interacting specifically with the histidines introduced at position −5′ or at position −2′. The electric distance (12) ($\delta = 0.7$; Fig. 7*I*) indicates that Zn^{2+} is bound deep in the pore, at a point 70% of the way across the electric field of the membrane in both chimeras, in accord with folding constraints (see *Model Building* in *Supporting Text*). The "equivalent valence" (12) of the open-channel block ($\delta z = 1.4$) indicates that during a blocking event, a single Zn^{2+} ion is present in the cross section of the pentagonal histidines' ring. Given the micromolar apparent affinities (Table 1) and the geometrical constraints in a planar pentagonal ring, Zn^{2+} likely forms Coulombic interactions with no more than two neighboring histidines simultaneously (see *Note 1* in *Supporting Text*). Consequently, Zn^{2+} becomes partially dehydrated. Hence, the incapacity of Zn^{2+} to block chimera H+16′ (Table 1) implies that the distance between neighboring histidines at position 16′ is larger than the distance between neighboring histidines introduced at position 9′, 2′, −1′, −2′, or −5′.

Functional and Structural Implications of the Off-Response Currents. We attribute the off-response phenomenon to the following process. At −80 mV, washout of an open-channel blocker would relieve the channel from block and would enable brief ionic flow before the channel closes. Indeed, inward-current blips were observed upon washout here (e.g., Fig. 1*B*) and also in the muscle AChR upon washout of QX-314, a quaternary ammonium

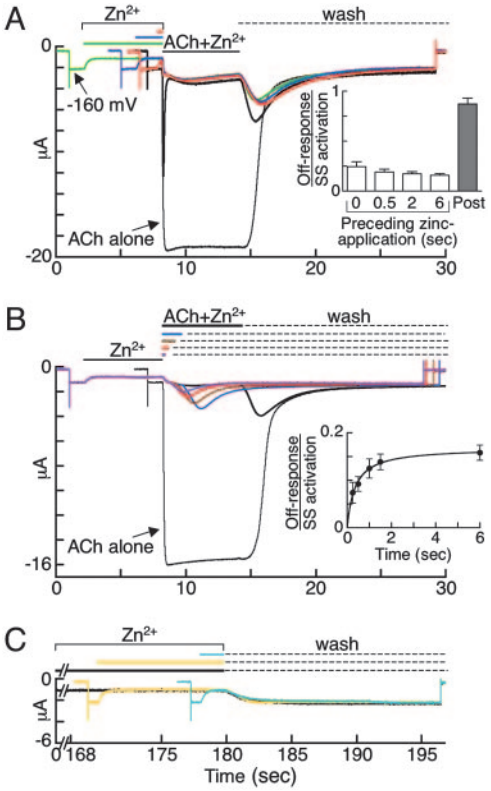

Fig. 3. Effects of Zn^{2+} applied externally before activation of chimera H−2′. (*A*) Application of Zn^{2+} (1 mM) for 0.5 (red), 2 (blue), and 6 (green) s is followed by coapplication of ACh (300 μM) together with Zn^{2+} (1 mM). Black trace corresponds to coapplication without preceding application of Zn^{2+}. Dashed line corresponds to a wash with ND 96. (*Inset*) The ratio of off-response peak current over steady-state (SS) activation (ACh alone, gray trace) in relation to the time of Zn^{2+} application before the coapplication (open bars). The gray bar (Post) corresponds to the same ratio obtained in Zn^{2+} postapplication experiments (e.g., Fig. 2*B*, blue trace). (*B*) Application of Zn^{2+} (1 mM) for 6 s is followed by varying periods of coapplication of ACh (300 μM) plus Zn^{2+} (1 mM): purple, 0.25 s; red, 0.5 s; brown, 1 s; blue, 2 s; black, 6 s. In *Inset*, data were fitted with a nonlinear regression to Eq. **3** in *Supporting Materials and Methods* in *Supporting Text*. (*C*) Preapplication of Zn^{2+} for 2, 10, and 180 s is immediately followed by washout. All currents were recorded at −160 mV. Traces shown in *A* and *C* are from the same oocyte; the traces in *B* are from another oocyte, demonstrating the reproducibility of the currents' proportionalities. Experiments shown in *A* and *B* were repeated independently seven times; the error bars in *Insets* correspond to their SD values. Results shown in *C* were repeated independently five times.

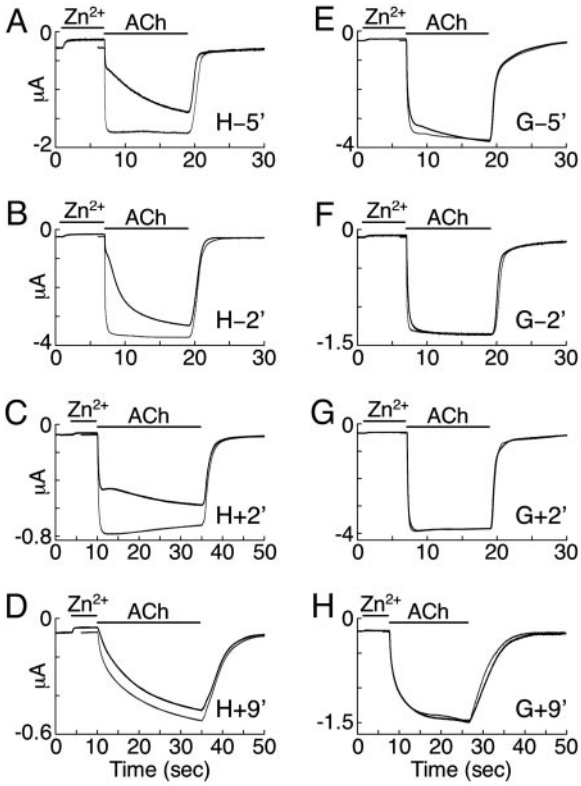

Fig. 4. Effects of preceding application of Zn^{2+} on activation time courses. (*A–H*) External application (6 s) of 1 mM Zn^{2+} is followed by application of 300 μM ACh alone (black traces) to oocytes expressing the depicted chimeras. The gray traces correspond to activation by ACh without preceding application of Zn^{2+}. Time constants of activation are provided in Table 2.

anesthetic derivative that acts as an open-channel blocker (13). In contrast, at extremely negative membrane voltages, the strong electric force drives Zn^{2+} ions into the pore, thereby counteracting the tendency of unbound Zn^{2+} ions to diffuse out of the pore (due to the washout). These opposing forces cause Zn^{2+} ions to bounce repeatedly in and out of the engineered metal-binding site until Zn^{2+} ultimately leaves the pore. When an unbound Zn^{2+} ion moves above its binding site, it cannot block the pore. Taken together, washout at very negative membrane voltage would result in channels that fluctuate between open blocked (OB) and open (O) states giving rise to large macroscopic inward currents, which reflect ionic flow between blocking events. Given that, before washout, most of the population is shifted to the OB state and that, upon washout, this population enters into OB↔O fluctuation, the macroscopic inward currents could become larger than the steady-state currents (Fig. 2 *B–E*).

Although we did not perform single channel recordings (see *Note 4* in *Supporting Text*), our interpretations are inspired and supported by the studies of Neher and Steinbach and Lester and colleagues (14–16), who showed that, upon exposure of a single AChR channel to an open-channel blocker (QX-222) at −150 mV, the channel is fluctuating between OB and O states and conducts between blocking events with the same conductance as in the absence of QX-222. Note that in our case, the outflow of Cl^- ions, which corresponds to most of the measured inward current at very negative voltages, probably facilitates the off responses (see Fig. 9 and *Note 3* in *Supporting Text*, which are published as supporting information on the PNAS web site).

We exclude the possibility that off responses occur because of slow dissociation of ACh *per se* because (*i*) if ACh retention had caused off responses, the off-response currents would have never exceeded the steady-state currents elicited by saturating ACh concentrations (Fig. 2 *B–E*) and (*ii*) the off responses increase linearly with hyperpolarization (Fig. 2*F*), indicating that this phenomenon originates inside the pore. Note that the incapacity of the Gly-containing controls to display off responses (Fig. 8) indicates that Zn^{2+} must interact specifically with histidines introduced in the pore to generate off responses.

Because the off responses are seen when His is introduced at position −5′, −2′, −1′, 2′, or 9′, no local rearrangements that might occlude the pore take place above or below these positions. It is thus most likely that the pore-lining segments move rigidly during gating.

Extracellular Zn^{2+} Has Accessibility to the Bottom of the Resting (Closed) Pore. The transient currents observed upon coapplication of ACh plus Zn^{2+} represent opening of channels that instantaneously become blocked by Zn^{2+} (Fig. 3*A*). The complete disappearance of these transient currents and the drastic

reduction in off responses when Zn^{2+} is externally applied before coapplication (of Zn^{2+} plus ACh) (Fig. 3 *A* and *B*) indicate unambiguously that external Zn^{2+} gets access to the bottom of the resting (closed) pore and prevents channels' opening.

We exclude any possibility of effective accumulation of spontaneously OB channels during the application of Zn^{2+} alone (i.e., before the addition of ACh) for the following reasons. (*i*) Off responses are not seen when washout is performed immediately after prolonged application of Zn^{2+} alone (Fig. 3*C*). This finding indicates that Zn^{2+} alone cannot shift the equilibrium toward the OB state, which is capable of producing off responses. (*ii*) Preceding application of Zn^{2+} reduces the off responses by ≈80% (Fig. 3*A Inset*). Because the off responses serve as a measure of the open-state population (i.e., OB↔O fluctuation), the drastic reduction in the off responses indicates that application of Zn^{2+} before activation stabilizes at least ≈80% of the population in a closed-blocked state that is not capable of producing off responses. Spontaneous opening cannot even be a source for open-channel block of the remaining ≈20% fraction because the small, slowly progressing inward current and its following small off response appear only when adding ACh, which triggers opening of channels that in turn become blocked (Fig. 3 *A* and *B*). (*iii*) In Fig. 4 *A–C* (performed at −80 mV), Zn^{2+} is washed out during the beginning of the ACh application phase, yet the activation rate is slow and does not return to a fast rate even after 12 s. This slow activation phase is prolonged despite the fact that, at −80 mV, washout of OB channels for 2–4 s (i.e., in postapplication protocols) enables reactivation with fast kinetics (as is typical of the control gray traces seen in Fig. 4 *A–C*). Conclusively, the slow activation rates shown in Fig. 4 *A–C* cannot be related to spontaneously OB channels; instead, they reflect channels that cannot readily open because of tight binding of Zn^{2+} at the bottom of the resting pore. Taken altogether, our results unequivocally prove that the activation gate is actually a constriction that occupies a cytoplasmic location. This conclusion is in accord with that of Karlin and Wilson (8) and contradictory to previous interpretations (17) (see *Note 5* in *Supporting Text*).

Our results are also not in line with the EM studies that described a midpore hydrophobic girdle, which is made of two successive hydrophobic rings (positions 9′ and 13′) and was said to act as a barrier obstructing the passage of hydrated ions (6). The arguments against the hydrophobic girdle hypothesis are as follows. (*i*) All of the chimeras containing histidines between positions −5′ and 2′ rapidly close their gate, despite having a threonine at position 13′ (e.g., Fig. 6*D Right*; traces of ACh alone in Fig. 1 *A*, *B*, *D*, and *E*; and all traces in Fig. 4 *A–C* and *E–G*). (*ii*) Zn^{2+}, which, compared with Cl^- and Na^+, has a very low enthalpy of hydration (−505 kcal/mol) and a much slower rate of exchange of the inner water shell, easily passes through the midpore of chimeras H−5′, H−2′, and H+2′ and gets to the bottom of the resting pore despite the hydrophobicity at position 9′ (Figs. 3 *A* and *B* and 4 *A–C*). (*iii*) Chimeras H+9′ and G + 9′ harbor polar combinations at positions 9′ and 13′ (see Table 1), which completely eliminates the capacity of this region to act as a hydrophobic barrier, but these chimeras can close their gate (Fig. 4 *D* and *H*). (*iv*) If a hydrophobic girdle were stabilizing the closed state, as argued by Miyazawa *et al.* (6), its elimination in chimeras H+9′ and G+9′ should have resulted in fast opening; however, these chimeras open very slowly (Fig. 4 *D* and *H*). See also *Note 6* in *Supporting Text*.

The Conformation of the Resting (Closed) Pore. An initial homologous model was built by using the 3D structure of the membrane-embedded domain of the *Torpedo* AChR (6) as a template. Then, the orientation of the pore-lining segments was rigidly modified based on the capacity of Zn^{2+} to stabilize, when applied before activation, the closed-blocked resting state depending on the histidines' location (see *Model Building* in *Supporting Text*).

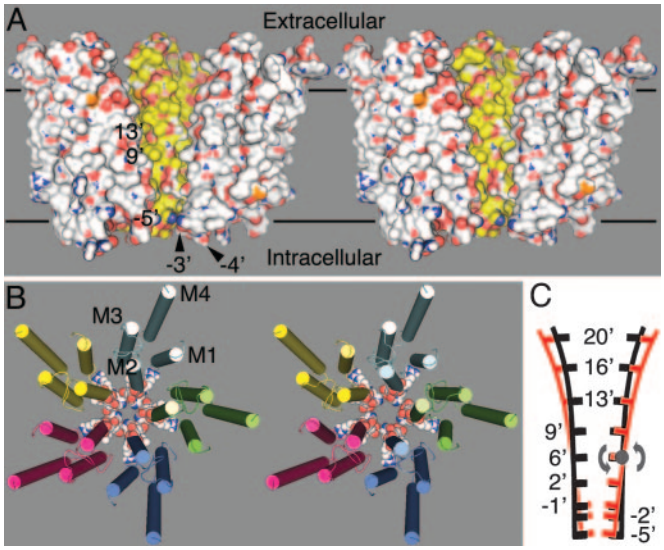

Fig. 5. Conformations and gating mechanism of a Cys-loop receptor pore. (*A*) Molecular surface of the membrane-embedded domain of chimera H−5′ displaying closed (*Left*) or open (*Right*) pore conformations, as viewed from within the membrane. For better viewing, the two frontal subunits have been removed; the carbons of the rear and frontal subunits are colored yellow and white, respectively. In all three subunits, oxygen, nitrogen, sulfur, and hydrogen atoms are colored red, blue, orange, and white, respectively. The black horizontal lines delineate the putative location of the membrane. Image was prepared with PYMOL. (*B*) Top view of the closed (*Left*) vs. open (*Right*) constriction as seen from the extracellular milieu. The residues from position −5′ to position 2′ are shown as space-filling spheres; carbon, nitrogen, oxygen, and hydrogen atoms are colored white, blue, red, and white, respectively. Note that the side chain of the conserved basic amino acid at position 0′ points outward from the permeation pathway (see also *Note 3* in *Supporting Text*). The helical transmembrane segments (four per each of five differently colored subunits) are shown as cylinders. Image was prepared with PYMOL. (*C*) 2D schematic side view corresponding to the proposed gating motions, as shown for two facing subunits. Red and black lines represent the closed and open states, respectively. The plausible axis of tilting (shown as a gray ball) is perpendicular to the viewer and is located between positions 2′ and 9′. The gray arrows indicate the motions around this point, which remains fixed during tilting.

Our model displays a pore lumen shaped as an inverted teepee (Fig. 5*A Left*). The five pore-lining segments adopt an oblique orientation relative to the axis of ion conduction and create a constriction at the bottom of the pore (most intracellularly), which keeps the channel closed at rest (Fig. 5 *A Left* and *B Left*). At its middle, the pore is sufficiently wide to enable hydrated ions to pass the midpore, in line with the observation that Zn^{2+} does not inhibit chimera H+9′ when it is applied before activation. A plausible reason for the difference between the activity-dependent orientation of the pore-lining segments (in the current study) and the orientation deduced from electron microscopy (6) is discussed in *Note 7* in *Supporting Text*.

The Conformation of the Active (Open) Pore. The capacity of Zn^{2+} to stabilize the OB state depending on the position of the histidines allowed us to model the open state, as well. This process (see *Supporting Materials and Methods* in *Supporting Text*) gave rise to a smaller tilt of the pore-lining segments (Fig. 5*B Right*). Consequently, compared with the closed state (Fig. 5*A Left*), the lumen of the open pore (Fig. 5*A Right*) is wider at its bottom and narrower at its upper part. Yet, the cytoplasmic vestibule remains the narrowest part of the pore in both the closed and the open states, in accord with Panicker *et al.* (17).

Our open-pore structure is compatible with the inability of Zn^{2+} to block chimera H+16′ and with the capacity of Zn^{2+} to block the open channel and to produce off responses by interacting specifically with histidines substituted at position −5′, −2′, −1′, 2′, or 9′ (Table 1 and Fig. 2 *A–E*).

The open-pore structure also implies that in its upper part, the water serves as a high dielectric medium, whereas a potential drop appears mostly across the lower part of the pore, which is narrower, in line with our findings that Zn^{2+} ions have to pass 70% ($\delta = 0.7$) of the electric field of the membrane to interact with histidines introduced at the bottom of the pore (Fig. 7*I*).

A Plausible Gating Mechanism. The structural basis for coupling between motions in the neurotransmitter-binding domain and pore gating is still largely unknown (18–20). The distinct activity-dependent orientations of the M2 segments and the superposition of the closed- over the open-pore model provide further insights into principal gating motions. Pore-opening tilting of M2 around a point fixed between positions 2′ and 9′ (Fig. 5*C*, black) would bring position 9′ closer to the axis of ion conduction and neighboring L9′ residues closer to one another, in line with the observation that the open H+9′ mutant is capable of binding Zn^{2+}. This finding is in accord with previous ones that showed that L9′ of the β- and δ-subunits of the muscle AChR strongly interact with each other in the open state (21): findings that do not reconcile with a closed-state girdle alleged to be broken apart upon opening (6). Concerted rigid-body tilting of the five M2 segments would move the M1–M2 loop (and position 2′) away from the axis of ion conduction to enable widening/opening of the bottom-pore constriction. Inverse tilting would reform the constriction at the bottom of the pore and would close the channel (Fig. 5*B*). It is therefore most likely that the disruption of interactions between neighboring M2 segments at the level of L9′ impairs the capacity of the five M2 segments to move smoothly together to widen the bottom-pore constriction. Deactivation, which would likewise require concerted tilting movements of the M2 segments, was also found to be slow (Fig. 4 *D* and *H*). We do not exclude twists or slight rotations as suggested for the α7 (22) and $GABA_A$ receptors (7), which might accompany the tilting motions that predominantly open and close the bottom-pore constriction.

Several studies have suggested that motions in the ligand-binding domain affect the pore conformation through residues that precede M1 (23, 24) and by means of interactions between loops of the neurotransmitter-binding domain and the M2–M3 loop (25–29). Hence, the aforementioned rigid tilting motions can be reasonably achieved by simultaneous movements of the N-terminal tip of M1 and the C-terminal tip of M2 toward or away from the axis of ion conduction.

Y.P. thanks the Center for Absorption in Science (Israel) for a fellowship. This work was supported by the Israel Science Foundation, the U.S.–Israel binational Science Foundation, a Recanati grant (to B.A.), Collège de France, Centre National de la Recherche Scientifique, Association pour la Recherche Contre le Cancer, and European Economic Community contracts.

1. Changeux, J.-P. (1990) in *Fidia Research Foundation Neuroscience Award Lectures* (Raven, New York), Vol. 4, pp. 21–168.
2. Betz, H. (1990) *Neuron* **5,** 383–392.
3. Karlin, A. (2002) *Nat. Rev. Neurosci.* **3,** 102–114.
4. Lester, H. A., Dibas, M. I., Dahan, D. S., Leite, J. F. & Dougherty, D. A. (2004) *Trends Neurosci.* **27,** 329–336.
5. Unwin, N. (1995) *Nature* **373,** 37–43.
6. Miyazawa, A., Fujiyoshi, Y. & Unwin, N. (2003) *Nature* **423,** 949–955.
7. Horenstein, J., Wagner, D. A., Czajkowski, C. & Akabas, M. H. (2001) *Nat. Neurosci.* **4,** 477–485.
8. Wilson, G. G. & Karlin, A. (1998) *Neuron* **20,** 1269–1281.
9. Wilson, G. & Karlin, A. (2001) *Proc. Natl. Acad. Sci. USA* **98,** 1241–1248.
10. Gibor, G., Yakubovich, D., Peretz, A. & Attali, B. (2004) *J. Gen. Physiol.* **124,** 83–102.
11. Eisele, J. L., Bertrand, S., Galzi, J. L., Devillers-Thiery, A., Changeux, J.-P. & Bertrand, D. (1993) *Nature* **366,** 479–483.
12. Hille, B. (2001) *Ion Channels of Excitable Membranes* (Sinauer, Sunderland, MA), 3rd Ed.
13. Pascual, J. M. & Karlin, A. (1998) *J. Gen. Physiol.* **112,** 611–621.
14. Neher, E. & Steinbach, J. H. (1978) *J. Physiol.* **277,** 153–176.
15. Charnet, P., Labarca, C., Leonard, R. J., Vogelaar, N. J., Czyzyk, L., Gouin, A., Davidson, N. & Lester, H. A. (1990) *Neuron* **4,** 87–95.
16. Leonard, R. J., Labarca, C. G., Charnet, P., Davidson, N. & Lester, H. A. (1988) *Science* **242,** 1578–1581.
17. Panicker, S., Cruz, H., Arrabit, C., Suen, K. F. & Slesinger, P. A. (2004) *J. Biol. Chem.* **279,** 28149–28158.
18. Chakrapani, S., Bailey, T. D. & Auerbach, A. (2004) *J. Gen. Physiol.* **123,** 341–356.
19. Celie, P. H., van Rossum-Fikkert, S. E., van Dijk, W. J., Brejc, K., Smit, A. B. & Sixma, T. K. (2004) *Neuron* **41,** 907–914.
20. Bourne, Y., Talley, T. T., Hansen, S. B., Taylor, P. & Marchot, P. (2005) *EMBO J.* **24,** 1512–1522.
21. Kearney, P. C., Zhang, H., Zhong, W., Dougherty, D. A. & Lester, H. A. (1996) *Neuron* **17,** 1221–1229.
22. Taly, A., Delarue, M., Grutter, T., Nilges, M., Le Novere, N., Corringer, P. J. & Changeux, J.-P. (2005) *Biophys. J.* **88,** 3954–3965.
23. Hu, X. Q., Zhang, L., Stewart, R. R. & Weight, F. F. (2003) *J. Biol. Chem.* **278,** 46583–46589.
24. Castaldo, P., Stefanoni, P., Miceli, F., Coppola, G., Del Giudice, E. M., Bellini, G., Pascotto, A., Trudell, J. R., Harrison, N. L., Annunziato, L., *et al.* (2004) *J. Biol. Chem.* **279,** 25598–25604.
25. Langosch, D., Laube, B., Rundstrom, N., Schmieden, V., Bormann, J. & Betz, H. (1994) *EMBO J.* **13,** 4223–4228.
26. Lynch, J. W., Han, N. L., Haddrill, J., Pierce, K. D. & Schofield, P. R. (2001) *J. Neurosci.* **21,** 2589–2599.
27. Laube, B., Maksay, G., Schemm, R. & Betz, H. (2002) *Trends Pharmacol. Sci.* **23,** 519–527.
28. Kash, T. L., Jenkins, A., Kelley, J. C., Trudell, J. R. & Harrison, N. L. (2003) *Nature* **421,** 272–275.
29. Bouzat, C., Gumilar, F., Spitzmaul, G., Wang, H. L., Rayes, D., Hansen, S. B., Taylor, P. & Sine, S. M. (2004) *Nature* **430,** 896–900.

Paas *et al*. 10.1073/pnas.0507599102.

Supporting Information

Files in this Data Supplement:

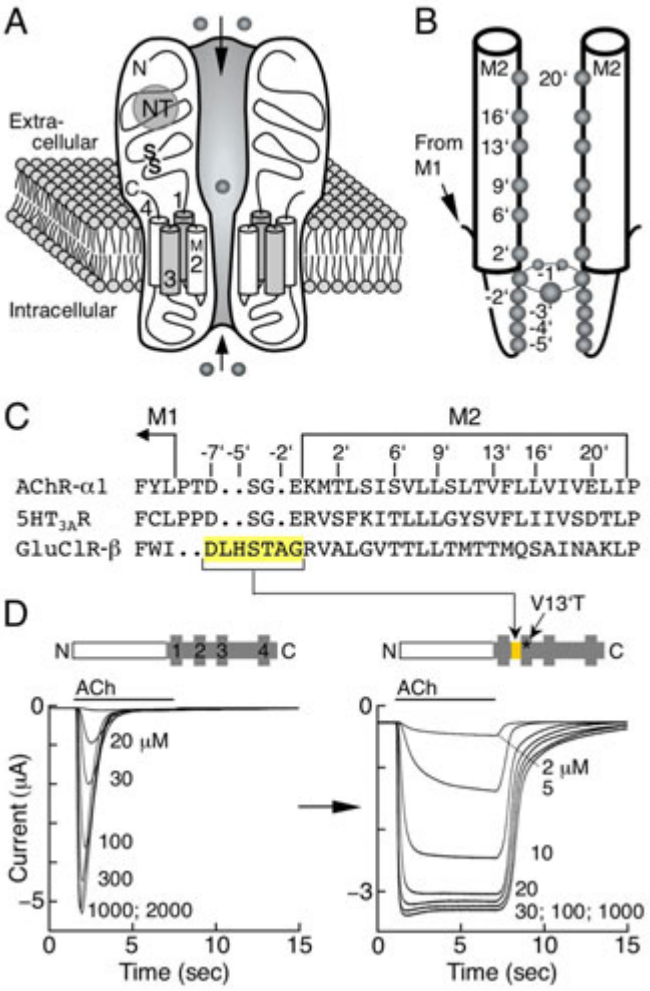

Fig. 6. General features of Cys-loop receptors. (*A*) Schematic side view of the receptor's channel. Two of five subunits were removed to expose the channel pore embedded in the lipid bilayer. All receptor subunits of this superfamily share the same transmembrane topology and similar amino acid sequences and display a completely conserved disulfide (S-S) bridge that creates the so-called Cys loop in their extracellular neurotransmitter (NT)-binding domain. The second transmembrane segment (M2) lines the channel pore. (*B*) A commonly accepted view of positions that carry side chains facing the permeation pathway (-1' to 20'). The primed numbers relate to the location relative to the position commonly considered as the first residue of M2. The residues corresponding to the numbered positions are shown in *C*. (*C*) Amino acid sequence alignment of three subunits of Cys-loop receptors. Part of M1, the entire M2, and their connecting segment are shown. The dots, which correspond to gaps in the sequence, are also numbered as positions. α1, the α-subunit of the *Torpedo* nicotinic acetylcholine receptor (Swiss-Prot accession no. P02710); $5HT_{3A}R$, 5-hydroxytryptamine (serotonin)-activated cationic channel from mouse (Swiss-Prot accession no. P23979); GluClR-β, the β-subunit of a glutamate-activated chloride-selective channel from *Caenorhabditis elegans* (Swiss-Prot accession no. Q17328). (*D*) The upper part of *Left* shows a schematic representation of an α7-$5HT_{3A}R$ chimeric subunit, which harbors the amino-terminal segment of the α7 nAChR (white segment) fused to the transmembrane core domain and intracellular portion of the $5HT_{3A}R$ (gray segments). Typical acetylcholine (ACh)-elicited currents recorded in *Xenopus* oocytes that express the chimeric α7-$5HT_{3A}R$ are shown (*Left*). The decline of the amplitude seen in the presence of ACh reflects desensitization. *Right* shows nondesensitizing currents typical of chimera H-5', where part of the M1-M2 linker was replaced by the M1-M2 linker of the GluClR β-subunit (shown in yellow) together with a V13'T substitution. Horizontal bars above the current traces correspond to the time of application. ACh concentrations in μM are depicted within the panels. Currents were recorded at –

80-mV holding potential.

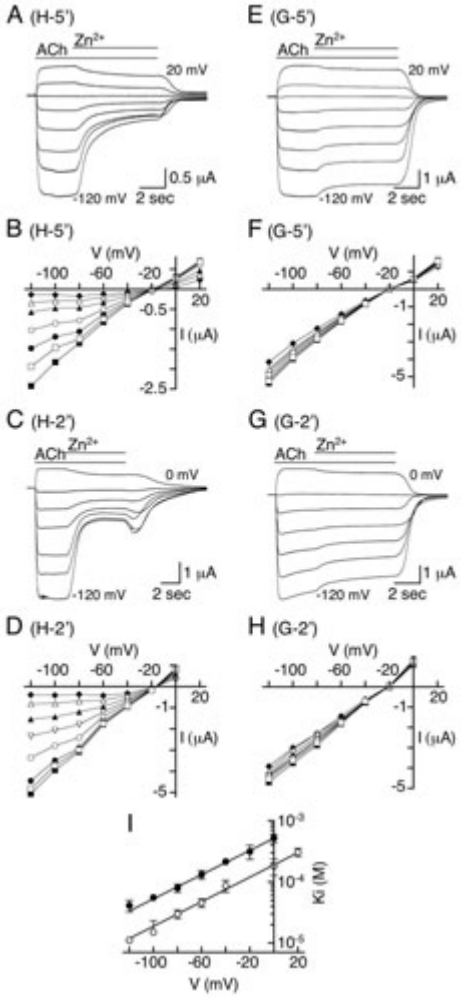

Fig. 7. Voltage dependence of inhibition by externally applied Zn^{2+}. (*A*, *C*, *E*, and *G*) Representative current traces corresponding to Zn^{2+} postapplication protocols recorded at various membrane voltages in 20-mV increments. ACh, 300 μM (saturating concentration); Zn^{2+}, 100 μM. (*B*, *D*, *F*, and *H*) *I-V* relations measured under various Zn^{2+} concentrations in μM: filled squares, 0; open squares, 1; filled circles, 5; open circles, 20; inverted open triangles, 50; filled triangles, 100; open triangles, 300; closed diamonds, 1,000. Chimeras' names are shown. (*I*) Zn^{2+} inhibition constant (K_i) plotted as a function of membrane voltage for mutants H-5' (open circles) and H-2' (filled circles). Data were fitted with a nonlinear regression to the Woodhull equation (see "Supporting Materials and Methods" in *Supporting Text*). Error bars correspond to SD of the mean of five independent experiments.

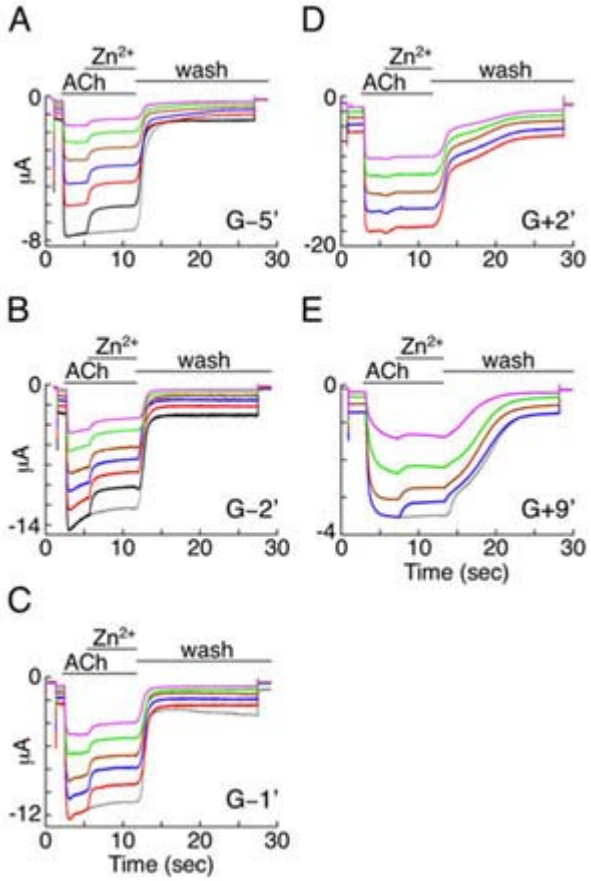

Fig. 8. Glycine-containing control mutants do not display off-response currents. (*A*-*E*) Representative current traces recorded for the indicated chimeras. ACh, 300 μM; externally applied Zn^{2+}, 1 mM; wash, physiological solution (ND96). The color codes for the holding voltages in mV are as follows: magenta, -100; green, -120; brown, -140; blue, -160; red, -180; black, -200. The gray traces correspond to steady-state activation currents elicited by ACh at -200 mV (*A* and *B*), -180 mV (*C*), and -160 mV (*E*). Experiments shown here were repeated independently at least five times.

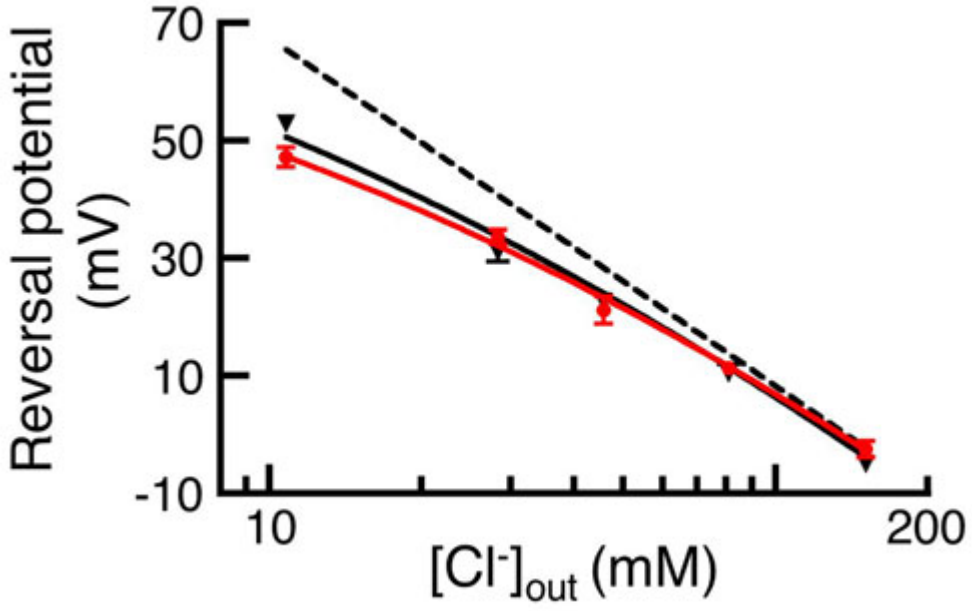

Fig. 9. Reversal potentials for the α7-GluClβ chimeric receptor (black triangles) and its single-site mutant, α7-GluClβR-R0'G (red circles). Reversal potentials were determined in transfected HEK-293 cells at different external Cl^- concentrations (see "Supporting Materials and Methods" in *Supporting Text*). Data were fitted with a nonlinear regression to the Goldman-Hodgkin-Katz equation implemented in PCLAMP (Axon Instruments):

$$Erev = \frac{RT}{F} \ln \frac{[Cl^-]_{in} + \alpha[Na^+]_{out} + \beta[Cs^+]_{out}}{[Cl^-]_{out} + \alpha[Na^+]_{in} + \beta[Cs^+]_{in}}$$

where *R*, *T*, and *F* are the gas constant, the absolute temperature, and the Faraday's constant, respectively, and the permeability ratios correspond to $\alpha = P_{Na}/P_{Cl}$ and $\beta = P_{Cs}/P_{Cl}$. Error bars correspond to SEM of recordings made in 12 cells expressing the α7-GluClβR and 8 cells expressing the R0'G mutant. The dashed line corresponds to the hypothetical situation where P_{Na} and P_{Cs} are equal to zero. Permeability ratios are as follows: α7-GluClβR, P_{Cl}/P_{Na} = 59.7 ± 21.8 and P_{Cl}/P_{Cs} = 16.5 ± 1.8. α7-GluClβR-R0'G, P_{Cl}/P_{Na} = 16.7 ± 3.8 and P_{Cl}/P_{Cs} = 12.9 ± 2.8. Construction was as follows: The amino terminal segment of the AChR α7 subunit was fused to the first transmembrane segment of the β-subunit of the nondesensitizing GluClβR, as performed previously with the α7-$5HT_{3A}$R chimera (1). The resulting homomeric α7-GluClβR is activated by ACh but not by glutamate. Hence, the α7-GluClβR can be expressed in HEK-293 cells grown in serum-containing medium with no need of glutamate depletion to avoid cytotoxicity. The α7-GluClβR is readily expressed to high levels in HEK-293 cells, giving robust responses of 3.8 ± 2.4 nA. A single-site R0'G mutation was introduced as described in "Supporting Materials and Methods" in *Supporting Text*. The amplitudes of currents recorded from cells expressing the R0'G mutant were 0.8 ± 0.15 nA.

Table 2. Kinetics of activation before and after application of Zn^{2+}

Chimera	τ_1, ms*	τ_2, ms*	*N*	$\tau_{1(zinc)}$, ms†	$\tau_{2(zinc)}$, ms†	*N*
H– 5’	66 ± 15		15	109 ± 25	6,272 ± 658	7
H– 2’	74 ± 28		10	107 ± 35	2,475 ± 810	7
H+2’	134 ± 22		8	221 ± 28	15,181 ± 1,629	7
H+9’	561 ± 193	8,527 ± 3,872	10	1,050 ± 218	8,310 ± 2,784	8

N, number of determinations.

*Time constant of activation by ACh, in ms (e.g., gray traces in Fig. 4). ± corresponds to SD.

†Time constant of activation by ACh, which was determined immediately after the application of Zn^{2+} (e.g., black traces in Fig. 4).

Supporting Text

Supporting Materials and Methods

Mutagenesis and Preliminary Assessment of Expression Capacity. The complementary DNA encoding the α7-5HT_{3A}R chimera (1) was subcloned in plasmid pMT3 (adenovirus promoter) between the Not-I and Xho-I restriction sites. Two unique silent restriction sites, Sal-I and Kpn-I, were respectively introduced upstream and downstream the M1-M2 linker by oligonucleotide-directed PCR. These two restriction sites were used for exchanging synthetic M1-M2 linker hybrid "cassettes." Point mutations along the M2 segment were introduced with the QuikChange kit (Stratagene). Sequences of the cassettes and the mutated cDNA inserts were confirmed by DNA sequencing.

Before embarking on DNA injections to *Xenopus* oocytes and electrophysiological recordings, the constructs were introduced into human embryonic kidney (HEK-293) cells by the calcium phosphate precipitation technique, and binding of [^{125}I]-α-bungarotoxin (5 nM) to living cells was monitored in the absence or presence of 1 mM nicotine, as described in ref. 2. This rapid screen allowed us to assess whether the mutants can assemble and arrive at the cell surface as a complex harboring functional ligand-binding interfaces.

Oocyte Perfusion and Data Acquisition. Oocytes were placed into a 100-μl recording chamber (application bath) and were perfused with ND96 solution (96 mM NaCl/2 mM KCl/1 mM $MgCl_2$/5 mM Hepes-NaOH, pH 7.5) supplemented with 2 mM $CaCl_2$. Our perfusion system operates under controlled N2 pressure to enable highly reproducible and constant perfusion velocity of 3.5-3.9 ml/min. The latter was measured before and after each set of experiments to ensure that clusters of comparative experiments are performed under precisely the same perfusion rates. The exchange of solutions was performed by electronic valves (ALA-VM8, ALA Scientific Instruments), which are controlled by the computer to allow instantaneous solution exchange. A homemade manifold having

only a few microliters of mixing volume together with very narrow connecting tubes prevented any backward flow when pressure is electronically switched to another tubing. Taken together, the liquid in the application bath was completely replaced within 1.5-1.7 s. Whole-cell currents were recorded by using a GeneClamp 500 amplifier (Axon Instruments). Data acquisition was performed as described in ref. 3.

Selectivity Determinations in HEK-293 Cells. For selectivity determinations, HEK-293 cells were transfected with chimeras H-5', H-4', or H-2' together with a GFP, using the calcium phosphate method. Electrophysiological recordings were made 2-3 days after transfection, using the whole-cell patch–clamp technique. To determine ionic permeability ratios, current-voltage relations were established in various external solutions with and without 100 μM ACh as follows. Solution A: 140 mM NaCl/2.8 mM KCl/2 mM $CaCl_2$/2 mM $MgCl_2$/10 mM glucose/10 mM Hepes–NaOH, pH 7.3. Solutions B and C are as in solution A, but NaCl was replaced by increasing concentrations of mannitol (up to 290 mM) or sodium isethionate (up to 140 mM), respectively. Patch pipettes (1-2 MΩ) were filled with a solution containing 140 mM CsCl, 4 mM $MgCl_2$, 4 mM Na-ATP, and 10 mM Hepes–CsOH (pH 7.3). External solutions were delivered by a computer-driven valve-manifold fast-exchange system enabling solution exchange within 10 ms. Current-voltage relations were determined by two methods, as follows: (*i*) steady-state currents evoked by ACh (100 μM, 3 s) were measured at different holding potentials ranging from -100 to +50 mV and (*ii*) two inverted voltage ramps (from +50 to -100 mV in 200 ms) were applied 1 and 2 s after the beginning of a 3-s application of ACh, from an initial holding potential of -60 mV (i.e., after steady-state activation is obtained). Leak currents obtained by the same protocol, in the absence of ACh, were subtracted. Liquid junction potentials were corrected by using the PCLAMP 8.1 version of the JPCALC software (4). Permeability ratios for Na^+, Cs^+, and Cl^- were calculated by using the Goldmann-Hodgkin-Katz equations (see legend of Fig. 9).

Determination of Activation Rate. (Data are provided in Table 1.) In all chimeras, the current rise of the traces (like those shown in Fig. 1) was best fitted to two exponential time courses by using the equation: $y = A_1e^{(-t/\tau 1)} + A_2e^{(-t/\tau 2)} + C$, where A_1 and A_2 are the current amplitudes that correspond to the time constants τ_1 and τ_2, respectively, and C is the constant y-offset for each component, 1 and 2. However, except for two mutants, one time constant is provided in Table 1. This single-exponential time constant corresponds to at least 95% of the amplitude, whereas the time constant corresponding to the entrance of the current trace into steady state (e.g., into the plateau in Fig. 1) is irrelevant for the activation rate. In contrast, activation of mutants H+9' and G+9' is slow already from its onset, displaying two rate components (e.g., Fig. 4 *D* and *H*).

Equations

Hill equation: $I/I_{max} = 1 - \{1/[1 + 10^{\{(\log Ki - \log[Zinc])nH\}}]\}$,

where I is the current observed at steady-state inhibition; I_{max} is the current observed at steady-state activation; K_i is the Zn^{2+} concentration that inhibits 50% of the response; n_H is the Hill coefficient.

Woodhull equation: $K_i(V) = K_i(0)\exp(-z\delta VF/RT)$,

where $K_i(V)$ and $K_i(0)$ are the inhibition constants calculated as in Fig. 1*C* at a given membrane voltage and at a zero membrane voltage, respectively; z is the valence of the blocking ion; δ is the electric distance across the electric field of membrane at which Zn^{2+} ions become bound; V is the membrane voltage; F, R, and T are the Faraday's constant, gas constant, and the absolute temperature, respectively.

Eq. **3**: $Y/Y_{max} = T/(T_{1/2} + T)$,

where Y is the ratio of off-response peak currents (e.g., of the colored and black traces in Fig. 3*B*) over steady-state activation currents obtained by ACh alone (e.g., the gray trace in Fig. 3*B*); Y_{max} is the maximal ratio; T is the time of coapplication of Zn^{2+} plus ACh; and $T_{1/2}$ is the time of coapplication required to reach half-maximal ratio.

Model Building. As a preliminary step, the full-length amino acid sequence of the mouse $5HT_{3A}R$ (5) (Swiss-Prot primary accession no. P23979) was submitted (at http://ca.expasy.org/cgi-bin/niceprot.pl?P23979) for searching a homologous template in the SWISS-MODEL repository, a database for theoretical protein models. The search for homologous sequences of known 3D structures scored the A, B, C, and D chains of the *Torpedo* AChR (6) (PDB ID code 1OED) with the highest sequence match serving as templates. Hence, the target sequence corresponding to the membrane-embedded domain of chimera H-5', <PLFYAVSLLLPSIFLMVVDIVGFCLPPDLHSTAGRVSFKITLLLGYSTFLIIVSDTLPATIGTPLI was aligned with the AChR A chain by using CLUSTAL W and the alignment was submitted for automated comparative protein modeling via the SWISS-PROT alignment interface (7, 8) (http://swissmodel.expasy.org/SWISS-MODEL.html). Elimination of a gap of two amino acids in M4 of chimera H-5' sequence further optimized the helical structure of M4 to give an initial model structure. The rms differences (rmsd) between the Cα atoms of the initial model and the A chain of the AChR were 0.13 Å, 0.09 Å, 0.09 Å, and 0.08 Å for M1 (the first 27 atoms), M2 (26 atoms), M3 (26 atoms), and M4 (31 atoms), respectively. Using DEEPVIEW/SWISS PDB-VIEWER 3.7, the initial model structure was arbitrarily fused to the A chain of the water-soluble acetylcholine-binding protein (AChBP; PDB ID code 1I9B). The latter is a structural and functional homologue of the amino-terminal neurotransmitter-binding domain of nicotinic AChR α-subunits, and its x-ray structure was determined at high resolution (9, 10). The fused molecule was oligomerized around a fivefold symmetrical axis by 3D molecular fitting to the AChBP oligomer. The fusion and oligomerization steps were repeated until the lowest deviation from the Cα atoms of the *Torpedo* AChR was achieved and a perfect symmetry around the axis of ion conduction was obtained. Then, the loop connecting M2 to M3 was extended to include amino acids <PATIGTPLIG> and was built computationally with the Pdb-Viewer Loop Database. As such, the M2 was actually shortened by one helical turn. Note that the first proline residue of this loop is completely conserved throughout Cys-loop receptors, indicating an important structural role as noted by Lester *et al.* (11). Modeled as such, the M2-M3 connecting loop interacts with loops 2 (the β1-β2 loop) and 7 (the Cys loop) of the AChBP. Interactions between these loops were functionally probed in a $GABA_A$ receptor (12), AChBP-$5HT_3$R chimera (13), and GlyR-α1 (14). Then, the M1-M2 linker (PPDLHSTAG) was manually modeled as a loop structure to orient the side chains of positions –1' to –5' according to the differential capacities of Zn^{2+} to interact with the imidazoles engineered along this segment. Concomitantly, M2 together with M1 and the M1-M2 loop were rigidly oriented relative to the axis of ion conduction in a mode that takes into account the capacity of Zn^{2+} to stabilize the closed blocked and the open blocked states in dependence of the sites of histidine substitution. In modeling terms, our molecular ruler was set according to the following criteria. Whenever a Zn^{2+} ion could be docked at simultaneous distance of ~3 Å (center-to-center) from each Nε atom of two neighboring histidines, we assumed blocking capacity according to the plausible blocking mechanism described in the text. Under such a docking mode, the imidazoles' van der Waals surface could come into contact with the surface of a Zn^{2+} ion that enters between two neighboring histidines. Whenever these surfaces were not in contact, we assumed inability of Zn^{2+} to block. Such situations were observed when the simultaneous center-to-center distance between a Zn^{2+} ion and each Nε atom of two neighboring histidines was ~3.4 Å or greater. Note that folding constraints of the backbone dictate the placement of position –5' and position –2' on different sides of the M1-M2 loop's "U-turn," thereby rendering histidines introduced in these two positions to be almost at the same

topological height in the pore. This modeling observation is fully consistent with the finding that the electric distance [δ; (15)] across the electric field of the membrane at which Zn^{2+} ions become bound is the same for chimeras H–5' and H–2' (see Fig. 7*I* and the text).

Energy minimizations throughout the iterative modeling process were performed with the GROMOS96 implementation of Swiss-PdbViewer. The final closed and open structures (Fig. 5) display *in vacuo* energies of –22,380 and –22,900 KJ/mol, respectively. No clashes have been observed in both structures. Superposition of our closed and open pore final models reveals the following rmsd values: 2.16 Å for M1 (first 25 Cα atoms), 1.28 Å for the M1-M2 loop (9 Cα atoms), 1.46 Å for M2 (23 Cα atoms), 2.68 Å for the M2-M3 loop (10 Cα atoms), and 0.05 Å for the segment that includes M3, M4, and their connecting loop (67 Cα atoms). The rmsd values between the *Torpedo* AChR (6) and the transmembrane segments of the closed conformation of chimera H-5' are as follows: 4.07 Å for M1 (first 26 Cα atoms), 2.92 Å for M2 (23 Cα atoms), 0.65 Å for M3 (26 Cα atoms), and 2.92 Å for M4 (28 Cα atoms). The rmsd values between the AChR and the transmembrane segments of the open conformation of chimera H-5' are as follows: 2.31 Å for M1 (first 26 Cα atoms), 1.74 Å for M2 (23 Cα atoms), 0.65 Å for M3 (26 Cα atoms), and 2.90 Å for M4 (28 Cα atoms). These significant differences reflect the different placement of M1 and M2 around the axis of ion conduction as required based on the functional results, and a different placement of M4 necessary to prevent clashes with M1 and the Cys loop of the AChBP.

Note 1: Preliminary Considerations Related to Chimeric Design, Zn^{2+}-Protein Interactions and Glycine Substitutions as Controls. The α7-$5HT_{3A}$ chimeric receptor is a homopentameric channel having the pore domain of the $5HT_{3A}$R and is efficiently activated by acetylcholine (ACh) (1) (Fig. 6*D Left*). The M1-M2 linker of Cys-loop receptors is considered to contribute to the intracellular vestibule of the pore (Fig. 6 *A* and *B*). Replacing part of the M1-M2 linker of the α7-$5HT_{3A}$R by the M1-M2 linker of the GluClβR (Fig. 6*C*) resulted in: (*i*) transplantation of a histidine at position –5' and (*ii*) replacement of E–1' by Gly, which eliminated potential electrostatic interactions of Zn^{2+} with position −1' or coordination of Zn^{2+} by position −1' and a histidine introduced nearby. Then, the His residue was moved successively along the M1-M2 linker and introduced along M2 instead of residues considered to face the pore lumen of Cys-loop receptors (see sequences in Table 1).

Because the chimera used here is homomeric (like the native $5HT_{3A}$R), a mutation in one subunit at a position facing the pore lumen would generate a pentagonal ring with five substitutions organized symmetrically around the axis of ion conduction (as shown for position –1' in Fig. 6*B*). However, high-affinity coordination (dative covalent) bonds between Zn^{2+} and more than two histidines simultaneously was assumed impossible, although the His side chains may adopt different conformations. The reason is that the planar pentagonal ring of the histidines' Cα atoms actually prevents formation of a three-His site or a tetrahedral coordination geometry, which both require center-to-center simultaneous distance of ~3.2 Å between the imidazoles' Nε atoms themselves and of ~2.1 Å between the Zn^{2+} ion and each of the Nε atoms, as seen in various metalloproteins (16-18). Note that micromolar affinities of Zn^{2+} binding to two histidines are described in the literature (reviewed in refs. 16 and 17).

Receptor desensitization, which closes the channel immediately after activation while the neurotransmitter still occupies its binding site, was eliminated owing to a V13'T mutation known to abolish desensitization of the $5HT_{3A}$R (19) and other Cys-loop receptors (20). Removal of desensitization from the chimeras (Fig. 6*D Right* and all figures throughout) was essential to make certain that any current decline in the presence of Zn^{2+} could not be confounded with desensitization.

Glycine (Gly) residues, which cannot bind Zn^{2+}, were used to generate control mutants (Table 1). The rationale for using Gly substitutions as controls is as follows. (*i*) Although a Gly residue has more conformational freedom than any other amino acid, it is reasonable to assume that a single Gly substitution in M2 would not introduce drastic structural changes in the backbone because M2 is a helix having many interactions with its neighboring elements. Provided that the backbone is not affected, functional impairments owing to Gly substitutions in M2 can mostly be attributed to the loss of the bond network of the replaced residue. (*ii*) In loop structures, Gly introduces considerable flexibility. Introducing flexibility in the M1-M2 linker aimed at ensuring that the orientation of M1 and M2 with respect to each other would not be interrupted, so as to assure functional controls. Accordingly, all of the chimeras carrying Gly substitutions in the M1-M2 linker are expressed to high levels, giving robust responses with fast activation (see figures throughout and Table 1).

Note 2: The "Pathological Open-Desensitized State." The so-called "pathological open-desensitized state" was proposed for a homomeric AChR α7-L9'T mutant that displays no change in the Hill coefficient and ~160-fold increase in the apparent affinity to ACh, properties typical of a desensitized state (21). The latter phenotype was also observed when a mutation at position 9' of the heteromeric muscle AChR caused a drastic increase in apparent affinity with a Hill coefficient that decreased toward the value of 1.0 upon mutagenesis of more than two subunits (22).

Note 3: Changes in Charge Selectivity. Previous studies of various Cys-loop receptors have indicated that mutations in the M1-M2 linker change the charge selectivity (20, 23-25). Because we used the M1-M2 linker of a chloride-selective Cys-loop receptor (GluClβR), we examined the ionic selectivity of three representative chimeras. The permeability ratios were as follows. Chimera H-5', $P_{Cl}/P_{Na} = 3.3 \pm 0.6$ and $P_{Cl}/P_{Cs} = 2.2 \pm 0.1$; chimera H-4', $P_{Cl}/P_{Na} = 2.5 \pm 1.0$ and $P_{Cl}/P_{Cs} = 1.6 \pm 0.5$; chimera H-2', $P_{Cl}/P_{Na} = 4.5 \pm 0.1$ and $P_{Cl}/P_{Cs} = 2.9 \pm 0.6$. These ratios indicate that these chimeras lost their selectivity and became largely permeable to Cl^- ions.

We cannot exclude the possibility that this functional change is accompanied with a structural alteration owing to the bulkiness and electrostatic repulsion between the His side chains. However, it should be noted that most of the cationic Cys-loop receptor subunits (including the $5HT_{3A}R$'s pore that was mutated here) have at position –1' a negatively charged residue (E) that is almost as bulky as histidine (109 $Å^3$ vs. 118 $Å^3$, respectively). Given that position −1' is located at the narrowest part of the pore (26), one may analogically assume that electrostatic repulsion between histidines or their bulkiness do not considerably change the overall structure of the pore or principal gating motions. Note that in all of the chimeras used here, a Gly residue occupies position -1' [i.e., the native residue of the GluClβR (see Fig. 6*C* and Table 1)].

It was previously suggested that the residues composing the M1-M2 linker orient differently when the charge selectivity of the receptor is changed due to mutations in this segment. This suggestion was based on the hypothesis that in anionic (but not in cationic) Cys-loop receptors the basic residue at position 0' points to the pore lumen and interacts with the passing Cl^- ions (25). However, no experimental data that could substantiate this hypothesis have been brought to light thus far. On the contrary, the anionic homomeric ρ1 $GABA_AR$ remains mostly permeable to Cl^- after mutating R0' to methionine or cysteine ($P_{Na}/P_K/P_{Cl} = 0:0.11:1$ and $0:0.14:1$, respectively) (24). These observations indicate that positive charge at position 0' is not necessary for Cl^- permeability. To confirm these observations, we checked the charge selectivity of the GluClβR's pore after introducing a single R0'G mutation. This mutant remained Cl^--selective (Fig. 9), indicating that the side chain at position 0' does not have to point to the pore lumen to enable Cl^- permeability. These results and conclusion are in line with our structural models, where the folding of the M1-M2 loop and its connection to M2 (which are based on the His scan) give rise to an outward orientation of the side chain of R0' (Fig. 5*B*).

Note 4: Very Small Unitary Conductance Is Typical of the $5HT_{3A}R$. The unitary conductance of the $5HT_{3A}R$ or chimeric receptors having the pore and the intracellular part of the $5HT_{3A}R$ is too small to be resolved by single-channel recordings (13, 27). This can be overcome by a triple mutation (concomitant RRR→QDA substitutions) in the HA stretch of the M3-M4 intracellular segment (13, 27). Mutations in this stretch were shown to affect gating properties of the muscle AChR (28). Taken together, we preferred to avoid further complications owing to additional three drastic concomitant mutations and to rely on macroscopic currents that could readily indicate when the channels are open blocked or closed blocked (see the text).

Note 5. Panicker *et al.* (29) substituted cysteines (C) along the pore of the homopentameric $5HT_{3A}R$ and identified two distinguishable blocking mechanisms that involve the interactions of Cd^{2+} with the cysteines, when the pore is open. These were a rapidly reversible (nonpersistent) blocking mechanism and a persistent (coordination) blocking mechanism. Whatever the chemical grounds for these two different mechanisms, both types indicate blocking processes owing to the interactions of Cd^{2+} with the cysteines. As such, both blocking mechanisms should equally indicate accessibility of the metal ion to the site of cysteines. In their study, Panicker *et al.* (29) did not check whether Cd^{2+} can block, in a reversible (nonpersistent) mode, the closed state of mutants carrying Cys substitutions at positions topologically above position 2'. Hence, in our opinion, their results cannot substantiate the conclusion that in the closed state, externally applied Cd^{2+} cannot access positions deeper than (more cytoplasmic to) position 9'.

Note 6: Most Anioinic Cys-Loop Receptors Harbor a Hydrophilic Residue at Position 13'. With a few exceptions (around 3), all anionic Cys-loop receptor subunits cloned thus far (>100 subunits across various species) harbor a polar residue (mostly threonine) at position 13' (see the LGIC database). Additionally, hydrophobic-to-hydrophilic mutations at position 13' in the $5HT_{3A}R$ and in the α 7-AChR did not alter the capability of the receptor to close upon washout of the agonist (19, 20). Before any other consideration, these facts call into question the necessity of two successive midpore hydrophobic rings for creating an activation gate (6).

Note 7: Different Shapes of the Pore Lumen. The solvent-accessible surface of the pore lumen of our closed-pore structural model looks like an inverted teepee (Fig. 5*A Left*), unlike that of the EM structure, which looks like an hourglass (6). It should therefore be noted that in the course of our attempts to crystallize the *Torpedo* AChR (30), we examined the possibility of using Unwin's crystalline tubes as nucleated seeds. However, preparations such as those described by Unwin and colleagues [see Fig. 1 in Kubalek *et al.* (31)] were found, by stopped flow experiments, to contain mostly receptors displaying a high-affinity desensitized state considered to have a closed channel. Taking into account these observations together with the study of Wilson and Karlin (32), who showed that extracellular methanethiosulfonates cannot pass the midpore of the desensitized state, we conclude that the structure presented by Unwin and colleagues (6) likely reflects a desensitized state rather than the resting state.

1. Eisele, J. L., Bertrand, S., Galzi, J. L., Devillers-Thiery, A., Changeux, J.-P. & Bertrand, D. (1993) *Nature* **366,** 479-483.

2. Corringer, P. J., Galzi, J. L., Eisele, J. L., Bertrand, S., Changeux, J.-P. & Bertrand, D. (1995) *J. Biol. Chem.* **270,** 11749-11752.

3. Gibor, G., Yakubovich, D., Peretz, A. & Attali, B. (2004) *J. Gen. Physiol.* **124,** 83-102.

4. Barry, P. H. (1994) *J. Neurosci. Methods.* **51,** 107-116.

5. Maricq, A. V., Peterson, A. S., Brake, A. J., Myers, R. M. & Julius, D. (1991) *Science* **254,** 432-

437.

6. Miyazawa, A., Fujiyoshi, Y. & Unwin, N. (2003) *Nature* **423,** 949-955.

7. Schwede, T., Kopp, J., Guex, N. & Peitsch, M. C. (2003) *Nucleic Acids Res.* **31,** 3381-3385.

8. Guex, N. & Peitsch, M. C. (1997) *Electrophoresis* **18,** 2714-2723.

9. Brejc, K., van Dijk, W. J., Klaassen, R. V., Schuurmans, M., van Der Oost, J., Smit, A. B. & Sixma, T. K. (2001) *Nature* **411,** 269-276.

10. Celie, P. H., van Rossum-Fikkert, S. E., van Dijk, W. J., Brejc, K., Smit, A. B. & Sixma, T. K. (2004) *Neuron* **41,** 907-914.

11. Lester, H. A., Dibas, M. I., Dahan, D. S., Leite, J. F. & Dougherty, D. A. (2004) *Trends Neurosci.* **27,** 329-336.

12. Kash, T. L., Jenkins, A., Kelley, J. C., Trudell, J. R. & Harrison, N. L. (2003) *Nature* **421,** 272-275.

13. Bouzat, C., Gumilar, F., Spitzmaul, G., Wang, H. L., Rayes, D., Hansen, S. B., Taylor, P. & Sine, S. M. (2004) *Nature* **430,** 896-900.

14. Castaldo, P., Stefanoni, P., Miceli, F., Coppola, G., Del Giudice, E. M., Bellini, G., Pascotto, A., Trudell, J. R., Harrison, N. L., Annunziato, L., *et al.* (2004) *J. Biol. Chem.* **279,** 25598-25604.

15. Hille, B. (2001) *Ion Channels of Excitable Membranes* (Sinauer, Sunderland, MA), 3rd Ed.

16. Higaki, J. N., Fletterick, R. J. & Craik, C. S. (1992) *Trends Biochem. Sci.* **17,** 100-104.

17. Regan, L. (1995) *Trends Biochem. Sci.* **20,** 280-285.

18. Alberts, I. L., Nadassy, K. & Wodak, S. J. (1998) *Protein Sci.* **7,** 1700-1716.

19. Dang, H., England, P. M., Farivar, S. S., Dougherty, D. A. & Lester, H. A. (2000) *Mol. Pharmacol.* **57,** 1114-1122.

20. Galzi, J. L., Devillers-Thiery, A., Hussy, N., Bertrand, S., Changeux, J.-P. & Bertrand, D. (1992) *Nature* **359,** 500-505.

21. Revah, F., Bertrand, D., Galzi, J. L., Devillers-Thiery, A., Mulle, C., Hussy, N., Bertrand, S., Ballivet, M. & Changeux, J.-P. (1991) *Nature* **353,** 846-849.

22. Labarca, C., Nowak, M. W., Zhang, H., Tang, L., Deshpande, P. & Lester, H. A. (1995) *Nature* **376,** 514-516.

23. Gunthorpe, M. J. & Lummis, S. C. (2001) *J. Biol. Chem.* **276,** 10977-10983.

24. Wotring, V. E., Miller, T. S. & Weiss, D. S. (2003) *J. Physiol.* **548,** 527-540.

25. Keramidas, A., Moorhouse, A. J., Pierce, K. D., Schofield, P. R. & Barry, P. H. (2002) *J. Gen. Physiol.* **119,** 393-410.

26. Wilson, G. G. & Karlin, A. (1998) *Neuron* **20,** 1269-1281.

27. Kelley, S. P., Dunlop, J. I., Kirkness, E. F., Lambert, J. J. & Peters, J. A. (2003) *Nature* **424,** 321-324.

28. Milone, M., Wang, H. L., Ohno, K., Prince, R., Fukudome, T., Shen, X. M., Brengman, J. M., Griggs, R. C., Sine, S. M. & Engel, A. G. (1998) *Neuron* **20,** 575-588.

29. Panicker, S., Cruz, H., Arrabit, C., Suen, K. F. & Slesinger, P. A. (2004) *J. Biol. Chem.* **279,** 28149-28158.

30. Paas, Y., Cartaud, J., Recouvreur, M., Grailhe, R., Dufresne, V., Pebay-Peyroula, E., Landau, E. M. & Changeux, J.-P. (2003) *Proc. Natl. Acad. Sci. USA* **100,** 11309-11314.

31. Kubalek, E., Ralston, S., Lindstrom, J. & Unwin, N. (1987) *J. Cell Biol.* **105,** 9-18.

32. Wilson, G. & Karlin, A. (2001) *Proc. Natl. Acad. Sci. USA* **98,** 1241-1248.